# Correlation between Structural, Chemical, and Electrochemical Properties of La$_{0.6}$Sr$_{0.4}$CoO$_{3-d}$ Nanopowders for Application in Intermediate Temperature Solid Oxide Fuel Cells

Leandro M. Acuña,[*,†,‡] Fernando F. Muñoz,[†,‡] and Rodolfo O. Fuentes[‡,§]

[†]DEINSO (Departamento de Investigaciones en Sólidos), UNIDEF-CITEDEF, J.B. de la Salle 4397, (1603) Villa Martelli, Buenos Aires, Argentina

[‡]CONICET, Buenos Aires, Argentina

[§]Departamento de Física, Centro Atómico Constituyentes, CNEA, Av. Gral. Paz 1499, (1650) San Martín, Buenos Aires, Argentina

Ⓢ *Supporting Information*

ABSTRACT: Lanthanum−strontium cobaltites are excellent mixed ionic and electronic conductors and exhibit good activity for the oxygen reduction reaction (ORR) at temperatures higher than 500 °C. This led to these materials being proposed as cathodes for solid-oxide fuel cell devices, either for the standard high temperature (SOFC, 900−1000 °C) or the intermediate temperature (IT-SOFC, 500−700 °C) range. Although it was determined that crystal structure and oxygen vacancies play a central role in these properties, little is known about cobalt speciation at SOFC or IT-SOFC working temperatures. In this study the cobalt speciation and local order of La$_{0.6}$Sr$_{0.4}$CoO$_{3-d}$ (LSC) is analyzed in detail for the first time in nano- and microstructured powders by means of in situ experiments using X-ray absorption spectroscopy (XAS) in the temperature range of 20−700 °C. The electrochemical performance of LSC-based cathodes in symmetrical cells under the same conditions is also studied using electrochemical impedance spectroscopy (EIS). Cobalt atoms can be found in any of the three possible oxidation states. Their relative amount depends on temperature and crystallite size. In crystallites of a few tens of nanometers, the ease with which Co atoms change their oxidation state is enhanced. This effect probably facilitates oxide transport in LSC-based cathodes.
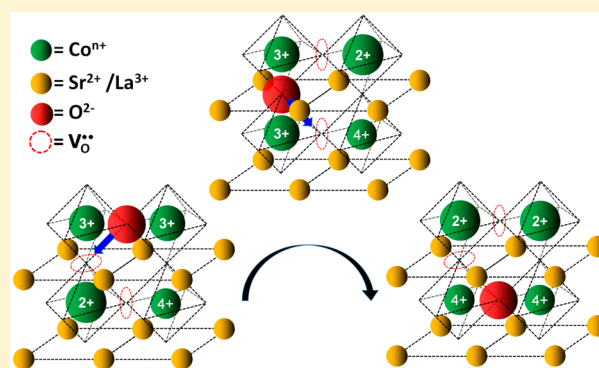
1. INTRODUCTION

Materials with perovskite structure have long been investigated due to their excellent electronic and ionic conduction properties, which make them suitable for application as electrodes in SOFCs (solid-oxide fuel cells). On the other hand, at the high working temperatures of SOFCs (800−1000 °C), several undesirable effects, such as further chemical reaction and diffusion, which affects the materials' structure, take place and reduce the SOFC's lifespan and performance. So, there is great interest in developing new materials for intermediate-temperature SOFC (IT-SOFC) devices, which can be operated between 500 and 700 °C.

The perovskite family (with formula ABO$_3$) is composed of a large number of members, of which LaMnO$_3$ was among the first to be investigated for application as a cathode, due to its high electronic conductivity at SOFC working temperatures, along with a considerable activity for the oxygen reduction reaction (ORR). The electronic conductivity is closely related to the perovskite crystal structure (*Pnma* space group for LaMnO$_3$), where the A-site is occupied by a lanthanide and the B-site by a transition metal. It has been shown that the crystal structure determines the crystal field, so small structural variations could have marked consequences on the electronic states of the transition metal.[1−5]

The discovery of mixed ionic-electronic conductors (MIECs) with perovskite structure represented a qualitative jump in cathode performance, as they offered their whole exposed surface to the gas phase as active sites for the ORR, a key step in cathode activity.[6] Substitution of the lanthanide by alkaline earths prompts oxygen vacancy formation, necessary for oxygen anion conduction from the active sites to the cathode/electrolyte interface. In contrast, in cathodes based on purely electronic high temperature conductors this reaction takes place only at the triple phase boundary (electrolyte/electrode/gas). The replacement of Mn on the B-site by other transition metals, such as Co, Fe, and Ni, has also been investigated. One of the most well-known examples is the La$_{1-x}$Sr$_x$CoO$_{3-d}$ family due to its high electronic and ionic conduction and thermodynamic stability under SOFCs operating conditions.[7]

Aliovalent doping at the A-site introduces effective charges that must be compensated by either oxygen vacancy formation (ionic compensation) or by changing the oxidation state of the B-site cation (electronic compensation). It should be noted that in materials with Co atoms filling the B-site, these two possibilities can occur at the same time.[8]

Although a large number of detailed studies have been performed on $La_{0.6}Sr_{0.4}CoO_{3-d}$ (LSC), focusing on synthesis, morphology, and structural, electrical, and electrochemical properties with a view to its use as a SOFC cathode, in no case were the chemical properties of the Co atoms in this material studied in detail under working conditions nor was it attempted to relate these to the electrochemical properties.[7,9−16] Nevertheless, it is assumed that many of the outstanding properties of LSC materials are based on the ease with which Co changes its oxidation state.

Considering nanostructured LSC powder (called hereafter LSC-nano) as a possible cathode material for IT-SOFC application, the aim of this work is to study in situ the Co speciation and its local order in LSC-nano under IT-SOFC cathode working conditions. The effect that crystallite size has on these properties is also studied by comparing these results to those obtained from conventional microstructured LSC powders (that will be referred to as LSC-micro). The electrochemical performance of LSC-based cathodes in symmetrical cells (cathode/electrolyte/cathode) is also studied in order to analyze the possible limiting processes at the cathode.

In summary, this work brings novel information about the Co speciation and local order in LSC powders under IT-SOFC working conditions and discusses the possible influence they have on the electrochemical processes taking place in an IT-SOFC cathode.

2. EXPERIMENTAL SECTION

2.1. Synthesis of LSC Powders. LSC powders were synthesized by the gel-combustion method, starting from $Sr(NO_3)_2$ (Aldrich, 99%), $La(NO_3)_3 \cdot 6H_2O$ (Aldrich, 99.999%) and $Co(NO_3)_3 \cdot 6H_2O$ (Aldrich, 98%).[17,18] Alanine ($C_3H_7O_2N$) (Merck, ≥99%) was used as the complexing agent and the fuel for the combustion step. Appropriate amounts of each nitrate were dissolved in distilled water separately and then mixed to obtain the desired stoichiometry. Alanine solution was added in order to achieve a stoichiometric combustion. The solution was then concentrated on a hot plate at 80 °C until it reached a 0.1 M concentration. The final solution was added, drop by drop, into a Pyrex vessel preheated and maintained at 300 °C, where it burnt rapidly, yielding a foamy black powder.[10] The powder was separated into two batches. The first one was calcined at 600 °C for 5 h in order to remove carbon and to obtain the desired nanostructured powders with the perovskite phase (LSC-nano). The other batch was treated at 1100 °C for 1h to obtain samples with microsized crystallites (LSC-micro).

2.2. Synthesis of Standards for XAS Experiments. To prepare a Co(III) standard for XAS experiments, $LaCoO_3$ powder was synthesized by adding citric acid (Aldrich, 99%) to the $La(NO_3)_3 \cdot 6H_2O$ and $Co(NO_3)_3 \cdot 6H_2O$ solution as a complexing agent, in a metal/acid molar ratio of 1:1. The solution was concentrated on a hot plate at 100 °C until a homogeneous gel was formed. The gel was calcined at 700 °C for 2 h.[19] $BaCoO_3$ (Co(IV) standard) was synthesized following the procedure described by Milt et al.[20] Finally, a commercial CoO powder was used as a Co(II) standard (Sigma-Aldrich, ≥99.99%).

2.3. Preparation of Symmetrical Cell for EIS. Dense electrolytes of 1 mm thickness and 10 mm diameter were obtained from commercial $Sm_{0.2}Ce_{0.8}O_{1.9}$ powder (SDC, NexTech Materials) uniaxially pressed under 20 kPa and then sintered in a tubular furnace at 1400 °C for 5 h. Slurries of LSC powders and DECOFLUX WB 41 (Zschimmer & Schwarz, Germany) vehicle were prepared in a 1:1 weight ratio. Thick films of area 0.24 cm^2 were then screen printed onto both faces of the SDC electrolytes and fired at 650 °C for 2 h. With this procedure cathodes of 30 μm thickness were achieved. Finally, silver paste was screen printed onto the cathode films and fired at 630 °C to serve as current collectors.

2.4. Characterization of LSC Powders. X-ray powder diffraction (XPD) was employed for preliminary structural characterization using a Philips PW 3710 diffractometer with Cu Kα radiation at room temperature (RT). Scans were collected in the range of $2\theta = 20-80°$ with steps of 0.02° and step counting time of 4 s. The morphology of LSC powders was studied with a scanning electron microscope, a Philips SEM 515. Specific surface area (SSA) was calculated by BET analysis employing a Quantachrome Autosorb 1-MP instrument using nitrogen as adsorbate. Analyses were performed after samples were degassed in vacuum at 200 °C for several hours.

2.5. SR-XRD Measurements. Synchrotron radiation X-ray diffraction patterns (SR-XRD) were collected at the D10B-XPD beamline of the Brazilian Synchrotron Light Laboratory (LNLS, Campinas, Brazil). The energy of the photon flux was set to 8 keV using a double Si(111) monochromator. Nominal photon flux at 7 keV was ~6 × 10^{10} photons·s^{-1}·$mrad^{-1}$ at 100 mA.[21] Powder diffraction reflections were collected with a Mythen 1K detector (DECTRIS).[22] Flat powder samples were loaded into a stainless steel sample holder and then placed inside a furnace with water refrigerated Kapton windows. Measurements were performed in static air between RT and 500 °C using the θ-2θ geometry in the range of $2\theta = 20-80°$ in the high-intensity mode, with steps of 0.01° and counting step time of 2 s. SR-XRD patterns were analyzed by means of the Rietveld's method using the Fullprof program.[23]

2.6. XAS Measurements. Experiments were carried out at the D04B-XAFS1 beamline of the LNLS.[24] Samples were prepared by mixing 8 mg of LSC powder with 42 mg of boron nitride in an agate mortar and then pressed into pellets of 13 mm diameter under uniaxial pressure of 2 kPa. The same procedure was applied to the standard samples. Pellets were placed inside a tubular furnace in a stainless steel sample holder. Furnace ends were closed with Kapton tape windows refrigerated with internal water flow. Measurements were performed in static air in transmission mode at the Co K-edge (7709 eV) with an energy resolution of $E/\Delta E \approx 25000$ at 7700 eV. The energy was selected with a Si(111) monochromator. The premonochromator slit was 0.3 mm in height. Ion chambers (one for the incident and two for the transmitted X-rays) were filled with nitrogen gas. The energy was calibrated with a metallic Co foil placed before the second transmitted X-ray ion chamber in order to measure both sample and reference at the same time. After 10 min stabilization, two XAS scans were recorded at 500 and 700 °C and averaged in order to improve the signal-to-noise ratio. This procedure also helped as a stability test for each sample.

XANES analyses where performed on the normalized spectra. The X-ray absorption coefficient, μ, was normalized following the standard data reduction procedure. The pre-edge region was fitted with a linear function and the post edge

region, 50 eV above the edge energy, E_0, with a second degree polynomial, setting as unity the values taken 1 keV above E_0. CoO, LaCoO$_3$, and BaCoO$_3$ samples were used as Co^{2+}, Co^{3+}, and Co^{4+} experimental standards for XANES analyses, respectively. Linear combination fitting (LCF) of these standards was performed in the energy interval 7.700−7.730 keV using the WinXAS 3.1 program, in order to characterize the relative abundance of cobalt species.[25,26] E_0 was determined as the absolute maximum of the first derivative of the normalized μ coefficient in the white line region or, equivalently, as the first zero of the second derivative of normalized μ in that region. E_0 values of the standards were employed to build up the energy calibration curve, used to determine the average oxidation state of Co atoms in the LSC samples.

The EXAFS signal, $\chi(k)$, was extracted from the $\mu(E)$ coefficient using the standard data reduction procedure and the WinXAS 3.1 program. EXAFS fitting was performed in the R space of the Fourier transform (FT) of $\chi(k) \times k^3$ between $R = 1.2$ and 4.0 Å (k = wavenumber) using the FEFFIT program.[27] EXAFS FT was calculated between $k = 3.6$ and 13.5 Å^{-1} using a Gaussian window. Phases and amplitudes for the different photoelectron paths were calculated by means of the FEFF 8.20 program.[28] The entry file for FEFF 8.20 was supplied from ATOMS 2.50 using the crystallographic information obtained from SR-XRD analyses.[29]

Different local order models were tested, starting with the simple and expected model derived from SR-XRD analyses. The first FT peak ($R = 1.2-1.9$ Å) was fitted separately in a first step, and then the fitting region was extended to the second peak, which includes the second and third coordination shells of eight A-site cations (La^{3+} and Sr^{2+}) and six B-site Co atoms, respectively. In all the cases the coordination number N_i of the ith shell was kept fixed. In the case of shells formed by cations, N_i was fixed to the nominal value calculated taking into account the chemical formula and the crystal structure. For the first shell, the existence of vacancies, which were estimated from the unit cell neutrality condition and chemical information about the oxidation states of Co atoms in each case (XANES), was also taken into account. In the case of the local order model that considers one different Co−O path length, R_{Co-O}, for every cobalt species, the scattering amplitude associated with each Co−O path was proportional to N_1 multiplied by the percentage weight of cobalt in each specific oxidation state. In this model it is supposed that all Co cations have the same N_1 and that vacancies are randomly distributed. This model is based on the assumption that, independently of whether the Co−O bond character is ionic or covalent, each cobalt oxidation state has a specific associated ionic or covalent radius.[30] So, each R_{Co-O} will be affected by the Co oxidation state.

For the second coordination shell it was necessary to use one R_{Co-La} path length for the Co−La path and another R_{Co-Sr} for the Co−Sr path. The final model also accounts for the coexistence of the three Co species in the third shell. As in EXAFS fitting it is mandatory to keep the number of variables as small as possible, only the three more relevant Co−Co paths were selected by means of their respective relative weight calculated from XANES results. Summarizing, one R path length for each subshell, one Debye−Waller factor (DW) for each shell and only one common E_0 shift (ΔE_0) for all the shells were used. In the final fitting a total of 12 variable parameters or less, with around 27 independent points, were

used. Low frequency background oscillation in k-space was also fitted with a seven knots spline function.

EXAFS fitting results obtained for the first coordination shell were tested by the bond valence method (BVM) as a first attempt for validating each model.[31−33]

The calculation of the oxygen occupation number, N_{occ}, for a given unit cell, using EXAFS results, was performed as a function of the difference $\delta R = d_{Co-O} - R_{Co-O}$ between Co−O distance calculated from SR-XRD analyses, d_{Co-O}, and R_{Co-O}. Considering oxygen anions as rigid spheres placed in $3c$ sites of the cubic or pseudocubic unit cell, with crystal radius $r_0 = 1.21$ Å[30] and volume $v_0 = 4/3\pi r_0^3$, the occupancy of the unit cell is given by

$$N_{occ} = N_1 \frac{v_{occ}}{v_0} \tag{1}$$

where

$$v_{occ} = \frac{\pi}{3}(r_0 + \delta R)^2 \cdot (2r_0 - \delta R) \tag{2}$$

is the volume occupied by the portion of the sphere inside a given unit cell.

CoO and BaCoO$_3$ standards were selected to get the passive electron reduction factor, S_0^2, as the coordination number N_1 of the nearest neighbor (NN) of cobalt is assumed to be known in these samples. The FT of $k^3\chi(k)$ of both standards were calculated using the same window in k-space (3.4−14.0 Å^{-1}). Then, the EXAFS FTs were fitted including the first to fourth coordination shells, fixing $N_1 = 6$ (the nominal value) and letting S_0^2 be free, along with R_i, DW$_i$, and ΔE_0 parameters.

2.7. Electrochemical Measurements. Electrochemical properties of LSC-based cathodes were studied by electrochemical impedance spectroscopy (EIS). Measurements were performed using the symmetrical cell configuration, cathode/electrolyte/cathode. EIS measurements were carried out using an Autolab PGSTAT302N instrument (Metrohm, Echo Chemie) in the temperature range of 400−625 °C under a synthetic air flow of 200 mL/min. The symmetric cells were excited with a sine wave of 50 mV amplitude in the frequency range of 0.02 Hz to 1 MHz sampling 10 points per decade on a log scale. The EIS spectra were fitted by means of the equivalent circuit method using the ZView 2 software (Version 3.0, Scribner Associates, Inc.).

3. RESULTS

3.1. Morphological and Structural Characterization. SEM images are presented in Figure SI1 as Supporting Information (SI) for LSC powders, as synthesized and at different thermal treatments. Synthesis yielded very foamy and porous black ashes, with thin walls, as can be seen in some broken bubbles in Figure SI1a. After calcination at 600 °C for 5 h the powder still exhibited the same characteristics as the as-prepared powder (Figure SI1b). On the other hand, when treated at 1100 °C for 1 h, nanoparticles were sintered, giving rise to microsized grains (Figure SI1c). In Figure SI1 it can be seen that, as the temperature of calcination increases, the porous character remains almost unaltered in the micro scale domain, but the porosity observed in the nanoscale domain is lost after calcination at 1100 °C.

Specific surface area decreased from 14 to 2 m^2·g^{-1} in powders treated at 600 and 1100 °C, respectively, which was expected from SEM analyses.

The reflections observed in patterns obtained by conventional XPD of LSC samples calcined at 600 °C (LSC-nano) and 1100 °C (LSC-micro) correspond to the rhombohedral (r) phase ($R\overline{3}c$ space group, No. 167, according to ICDS #82817).

3.2. SR-XRD Analysis. In Figure 1a,b is shown the SR-XRD patterns of LSC-micro at RT and 500 °C, respectively. The
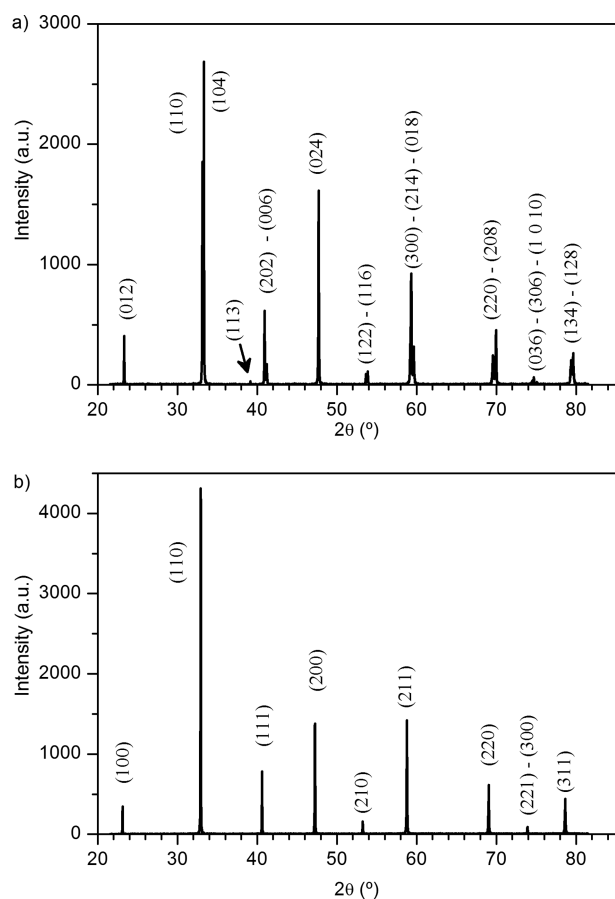

Figure 1. SR-XRD patterns of LSC-micro powder recorded at (a) room temperature with indexed reflections of the $R\overline{3}c$ space group and (b) 500 °C with indexed reflections of the $Pm\overline{3}m$ space group.

former exhibits the typical reflections of the r phase and the latter the reflections of the high temperature cubic (c) phase ($Pm\overline{3}m$ space group, No. 221, ICSD #86943).

In Figure SI2 are exhibited the SR-XRD patterns of LSC-nano at RT and 500 °C. Selected regions of LSC-micro powder SR-XRD pattern show the phase evolution as a function of temperature in Figure 2, between RT and 400 °C. At RT, the (110) and (104) reflections of the r phase are clearly resolved in Figure 2a. Angular separation between these reflections diminishes with increasing temperature, but up to 300 °C it is still possible to fit this peak with two pseudo-Voight functions. At 400 °C there is only one peak corresponding to the (110) reflection of the c phase. In Figure 2b the characteristic reflection (113) of the r phase as a function of temperature is shown. The integrated area of this peak is a function of the tilting angle (ϕ) of the oxygen octahedra. It should be emphasized that the small intensity of the (113) reflection is due to the low scattering cross section that oxygen atoms exhibit to X-rays. So, it is necessary to use neutron powder diffraction (NPD) to get more accurate estimates of the fractional coordinate x (and so, ϕ), of the oxygen located at (x,
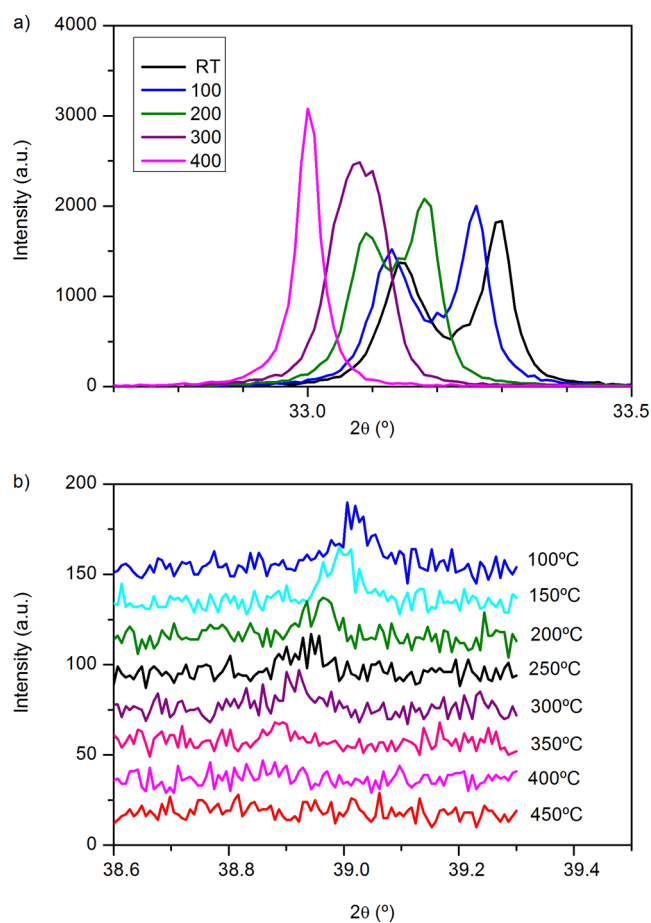

Figure 2. Selected regions of the SR-XRD pattern of LSC-micro at different temperatures. (a) (110) and (104) reflections; (b) (113) reflection. In this case, the patterns were vertically displaced for the sake of clarity.

0, 1/4) in the rhombohedral unit cell by means of the Rietveld's refinement method. It has to be taken into account that the Rietveld method assigns a low weight to the weaker reflections.

Nevertheless, using SR-XRD, it was possible to follow the evolution of this peak as a function of temperature for the LSC-micro powder (Figure 2b), due to the high photon flux of the source. Between 400 and 450 °C this reflection completely disappears. This indicates the $r \rightarrow c$ transition as this reflection is forbidden in the c phase. So, it is possible to affirm that LSC-micro undergoes an $r \rightarrow c$ phase transition between 400 and 450 °C. The SR-XRD pattern of LSC-nano powder exhibited the (110)−(104) splitting as a unique peak with an asymmetric peak profile at RT due to the peak broadening associated with the nanometric crystallite size. This broadening was used in the Scherrer formula to estimate the average crystallite size (D) of the powder to be about 30 nm.

At RT both powders exhibit the r phase, with slight differences in lattices parameters (Table 1). Another characteristic feature of the r phase is that A-cations are located at two slightly different distances from the Co atom on the B-site. In Table 1 is also included the difference $\Delta d_{\text{Co}-\text{La/Sr}}$, between both La/Sr subshells, in order to compare the strength of the rhombohedral distortion in both powders. $\Delta d_{\text{Co}-\text{La/Sr}}$ is smaller in the nanostructured powder. The lattice parameter a (r) is slightly shorter in LSC-nano, but c (r) and pseudocubic a' parameters are slightly longer in LSC-nano than in LSC-micro.

Table 1. Principal Results Obtained from the Rietveld Refinement Method Performed over SR-XRD Patterns of LSC-Micro and -Nano Powders

	LSC-micro[a] ($D > 300$ nm)		LSC-nano ($D = 30$ nm)	
	RT[b]	500 °C	RT	500 °C
SG[c]	$R\bar{3}c$	$Pm\bar{3}m$	$R\bar{3}c$	$Pm\bar{3}m$
a^{d} (Å)	5.430(1)	3.86656(3)	5.4282(1)	3.86745(7)
c^{e} (Å)	13.210(1)		13.2275(5)	
a'^{f} (Å)	3.8310(2)		3.8317(3)	
R_{p}	34.8	35.4	20.5	22.4
R_{wp}	48.5	54.8	14.1	14.9
R_{e}	20.0	25.2	8.58	7.49
χ^{2}	5.917	4.737	2.701	3.967
ϕ^{g} (deg)	7.1(5)	0	5.3(5)	0
$d_{Co-O}{}^{h}$ (Å)	1.925(1)	1.93328(2)	1.921(2)	1.93373(4)
$\Delta d_{Co-La/Sr}{}^{i}$ (Å)	0.02017(1)	0	0.01514(1)	0

[a]D: average crystallite size. [b]RT: room temperature. [c]SG: space group. [d]a: rhombohedral or cubic unit cell parameter. [e]c: rhombohedral unit cell parameter. [f]a': pseudocubic parameter. [g]ϕ: tilting angle. [h]d_{Co-O}: Co−O distance. [i]$\Delta d_{Co-La/Sr}$: difference in the distance between the two subshells of next nearest neighbors to Co.

At 500 °C the a (c) parameter is longer in LSC-nano. In this table the refinements are accompanied by reliability indices to judge the fitting quality. These indices are weighted R (R_{wp}), the reduced chi-squared (χ^{2}), and R_{e}, which are related just to the profile of the XRD patterns, and R_{p}, which is related to the crystal structure. The reduced chi-squared is defined as (R_{wp}/R_{e})^{2}, where R_{wp} is the index that should be analyzed to verify if the refinement is converging and R_{e} is the expected statistical value for R_{wp}.[34] They indicate that there is a poor agreement between the expected r phase and the SR-XRD pattern.

In Table 1 is also shown a coarse estimation of ϕ, based on the refinement's results on the fractional coordinate x. The tilting angle is calculated as tg(ϕ) = 2(x−0.5) 3$^{1/2}$.[9] The value of the x coordinate is also used in the calculation of d_{Co-O}, also included in the table. Calculations show that d_{Co-O} at RT is slightly shorter in LSC-nano. d_{Co-O} was used, in a first stage, as the initial value in the EXAFS fitting procedure and also as a reference value with which to compare the EXAFS fitting results.

3.3. XANES Analysis. The second derivatives of the Co−K edge XANES exhibit clear differences between LSC-micro and LSC-nano powders, while the edge absorption in LSC-micro seems to slightly shift to lower energies (Figures 3 and 4). It is commonly accepted that the profile of the white line and also the E_{0} value are due to the oxidation state of Co, while the degree of hybridization between Co-4p and O-2p orbitals determines the number of unoccupied states available for the 1s → 4p transition, which is, in turn, related to the area of the white line. Its shape also depends on the coordination. Good examples for this are the XANES spectra of CoO, LaCoO$_{3}$ and BaCoO$_{3}$ standards (Figure SI3).

The average oxidation state of Co atoms calculated by means of the calibration curve is nearly +3 in both powders and over the whole temperature range employed (Table 2).

The LCF method shows a very rich picture of the amounts of the different Co species (Table 3), which are sensitive to temperature changes and crystallite size, though the average oxidation state of Co is always close to +3, in accordance with the estimate from the calibration curve. This means that the
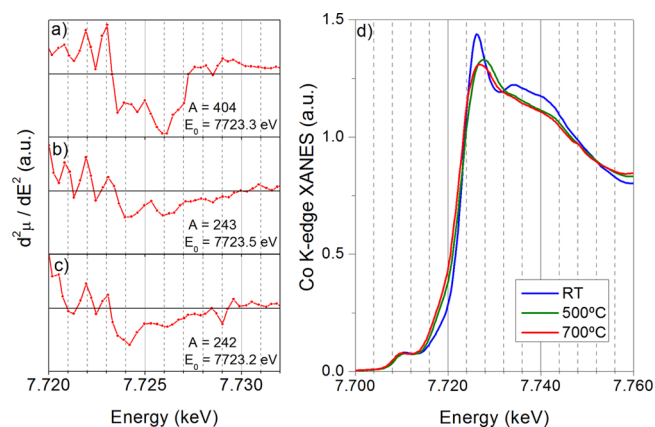

Figure 3. Second derivative of LSC-micro XANES spectra at the Co K-edge in the white line region at (a) RT, (b) 500 °C, and (c) 700 °C; A: mathematical area between zeros in arbitrary units; E$_{0}$: edge energy. (d) White lines of LSC-micro at different temperatures.
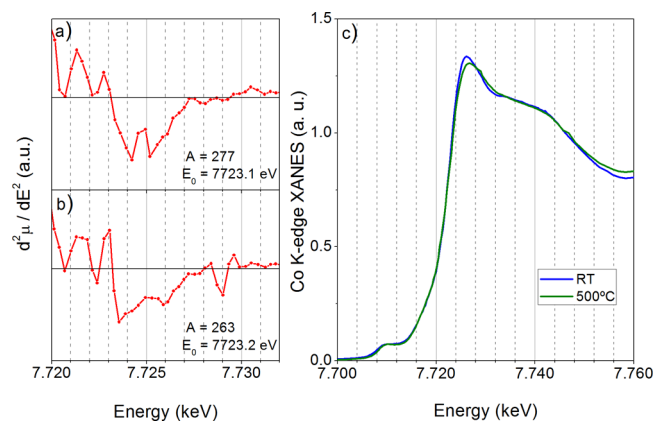

Figure 4. Second derivative of LSC-nano XANES spectra at the Co K-edge in the white line region at (a) RT and (b) 500 °C; A: mathematical area in arbitrary units; E$_{0}$: edge energy. (c) White lines of LSC-nano at different temperatures.

Table 2. Average Co Oxidation State of LSC-Nano and -Micro at Different Temperatures, Estimated from the Calibration Curve

sample	T (°C)	oxidation state
LSC-nano	20	+3.0(1)
	500	+3.0(1)
LSC-micro	20	+3.0(1)
	500	+3.1(1)
	700	+3.0(1)

latter method hides important information about the chemical properties of Co in LSC.

In Supporting Information, the low intensity edge structure previous to E_{0} (though misleading, for short, hereafter referred to as the pre-edge peak or pre-edge structure) of LSC-micro and -nano at different temperatures, along with the cobalt standards for +2, +3, and +4 oxidation states recorded at RT, are shown in detail (Figures SI4−SI6, respectively).[35]

3.4. EXAFS Analysis. As the fitting procedure performed on the EXAFS FTs of standard samples CoO and BaCoO$_{3}$ gave $S_{0}^{2} = 0.81(6)$ and $S_{0}^{2} = 0.9(2)$, respectively, S_{0}^{2} was fixed at 0.9 for the EXAFS fitting of LSC samples.

Table 3. Co Oxidation State and Content in LSC-Nano and -Micro Estimated from Linear Combination Fitting (LCF) Method at Different Temperatures

sample	T (°C)	oxidation state	content (%)	avg ox. state[a]
LSC-nano	20	+2	12(1)	
		+3	64(1)	3.1(4)
		+4	24(1)	
	500	+2	19(1)	
		+3	54(2)	3.1(5)
		+4	27(2)	
LSC-micro	20	+3	100(1)	3.00(3)
	500	+2	20(1)	
		+3	44(2)	3.2(3)
		+4	36(1)	
	700	+2	18(1)	
		+3	50(1)	3.1(3)
		+4	32(1)	

[a]Average oxidation state.

3.4.1. LSC-Micro at Room Temperature. A model with only one R_{Co-O} in the first coordination shell and also only one R_{Co-Co} in the third coordination shell best fitted the experimental data collected at RT (Table 4 and Figures 5a,b

Table 4. EXAFS Fitting Results for LSC-Micro at RT[a]

	Co−O	Co−La	Co−Sr	Co−Co
R (Å)	1.928(6)	3.34(1)	3.37(2)	3.94(2)
DW (Å²)	0.0047(3)	0.0039(6)	0.0039(6)	0.0040(8)
ΔE_0 (eV)	−7(2)	−7(2)	−7(2)	−7(2)

[a]Reliability factors: r-factor, 0.007; χ^2, 1046; reduced χ^2, 112.

and SI7), in agreement with the XANES analyses, where LSC-micro at RT was seen to have all of the Co atoms in the +3 oxidation state ($r_{Co} = 0.61$ Å)[30] and with the crystallographic r phase.

EXAFS analyses suggest that Sr^{2+} cations in the second coordination shell are located at a slightly longer distance from the absorbing Co than La^{3+} cations. The presence of two different path lengths for the second coordination shell is also in accordance with the r phase but it is expected that Sr^{2+} and La^{3+} cations occupy any of these sites randomly. This differentiation may be related to the fact that EXAFS is a chemically selective probe that can distinguish between atoms with different atomic number.

By means of the BVM, it was calculated that the effective average valence of Co is $V = 2.5$ (Table 5), significantly lower than that calculated by XANES analysis (calibration curve and LCF methods). But it can be said that, even so, they follow the same behavior as a function of temperature to that observed by XANES analysis.

3.4.2. LSC-Micro at 500 °C. Three subshells were needed for fitting the first peak in the EXAFS FT (Table 6 and Figures 5a and SI8), which totaled 5.87 oxygen atoms (as explained in section 2.6). The difference between the R_{Co-O} bond lengths and the values derived from Shannon's work is less than 6%.[30] The average R_{Co-O} is 1.98(5) ($>d_{Co-O} = 1.933$ Å). The average of the three R_{Co-Co} is 3.87(5) Å, very close to $d_{Co-Co} = 3.866$ Å. Interestingly, each R_{Co-Co} is double one of the R_{Co-O} bond lengths (Table 6 and Figure 5).

3.4.3. LSC-Nano at Room Temperature. One Co−O path and three Co−Co paths were employed to achieve a good
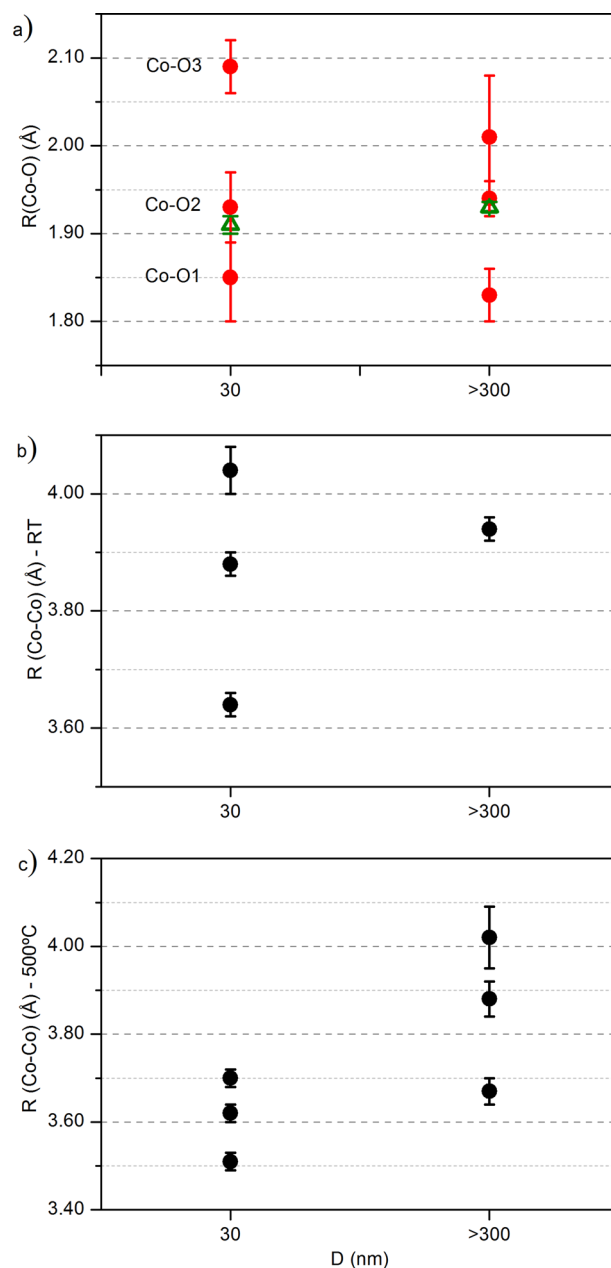
Figure 5. (a) EXAFS Co−O bond lengths of LSC-nano ($D = 30$ nm) and LSC-micro ($D > 300$ nm) at RT (green triangles) and at 500 °C (red circles). (b) Co−Co path lengths at RT. (c) Co−Co path lengths at 500 °C.

Table 5. Average Valence of Co Atom in LSC Powders, Calculated by Means of the BVM on the Basis of EXAFS Analysis

	temperature	
sample	RT	500 °C
LSC-micro	2.5	3.3
LSC-nano	2.9	2.9

quality of fit of the FT function (Figures 5a,b and SI9 and Table 7). The average $R_{Co-Co} = 3.82(2)$ Å, is close to the pseudocubic parameter a'. It is worth mentioning that the model with three oxygen subshells also yielded reasonable values for the fitting parameters but it was discarded as no

Table 6. EXAFS Fitting Results for LSC-Micro at 500 °C[a]

	Co−O	Co−La	Co−Sr	Co−Co
R (Å)	2.01(7)	3.18(3)	3.18(3)	4.02(7)
	1.94(2)			3.88(4)
	1.83(3)			3.67(3)
DW (Å^2)	0.0040(32)	0.0116(24)	0.0116(24)	0.0057(25)
ΔE_0 (eV)	−9(4)	−9(4)	−9(4)	−9(4)

[a]r-Factor: 0.038; χ^2: 1390; reduced χ^2: 166.

Table 7. Results of EXAFS Analysis on LSC-Nano at RT[a]

	Co−O	Co−La	Co−Sr	Co−Co
R (Å)	1.91(1)	3.13(3)	3.13(3)	4.04(4)
				3.88(4)
				3.64(2)
DW (Å^2)	0.0068(5)	0.0111(34)	0.0074(26)	0.0015(14)
ΔE_0 (eV)	−9(1)	−9(1)	−9(1)	−9(1)

[a]r-Factor: 0.016; χ^2: 4176; reduced χ^2: 491.

further improvement was achieved in the quality of the fit. In this model, the oxygen subshells have a smaller DW factor.

3.4.4. LSC-Nano at 500 °C. Three oxygen subshells were needed to fit the first FT peak (Figures 5a, SI10 and Table 8).

Table 8. Results of EXAFS Analysis on LSC-Nano at 500 °C[a]

	Co−O	Co−La	Co−Sr	Co−Co
R (Å)	2.09(3)	3.09(2)	3.11(2)	3.70(2)
	1.93(4)			3.62(2)
	1.85(5)			3.51(2)
DW (Å^2)	0.0026(15)	0.0029(13)	0.0004(2)	0.0036(16)
ΔE_0 (eV)	−9(1)	−9(1)	−9(1)	−9(1)

[a]r-Factor: 0.023; χ^2: 1406; reduced χ^2: 140.

Also, one subshell for La and another for Sr were used to fit the second peak, along with three Co subshells (Figure 5c). Average $R_{Co−O}$ is 1.94(1) Å and average $R_{Co−Co}$ is 3.60(2) Å.

3.5. Preliminary EIS Studies. The equivalent circuit model employed as a first approximation to the analysis of the EIS data consists of two series resistances R, each one in parallel with a constant phase element (CPE; Figure 6). These R//CPE subcircuits were used to fit the high frequency (HF) and the low frequency (LF) domains of the EI spectrum. The parallel R_eC_e element accounts for the grain boundary of the electrolyte and an additional R fits its pure resistive contribution. The CPE element is parametrized as $[T(i \cdot w)^P]^{-1}$, where T represents an ideal capacitance if $P = 1$, $i^2 = −1$ and w is the angular frequency.[36]

Nyquist plots for LSC-nano and -micro based cathodes show that the former has the smallest ASR in the studied temperature range (Figure 6b,c and Table 9). Also, E_a diminishes with diminishing D of the starting powders (Table 10).

The HF arcs in LSC-micro and -nano occur at roughly the same frequency (peak frequency at 500 °C: 380 and 204 Hz, respectively), and the P exponent exhibits different values, which seem to be temperature independent. In LSC-micro, $P \approx$ 0.5 over the whole temperature range but in LSC-nano, $P \approx$ 0.75.

The LF arcs also exhibit different peak frequencies (f_p), and P values. In LSC-micro, $P \approx 0.75$ (with $f_p = 1.7$ Hz at 500 °C), while in LSC-nano $P \approx 0.91$ (and $f_p = 38.9$ Hz at 500 °C). In relation to the latter case, it was found that porous or rough
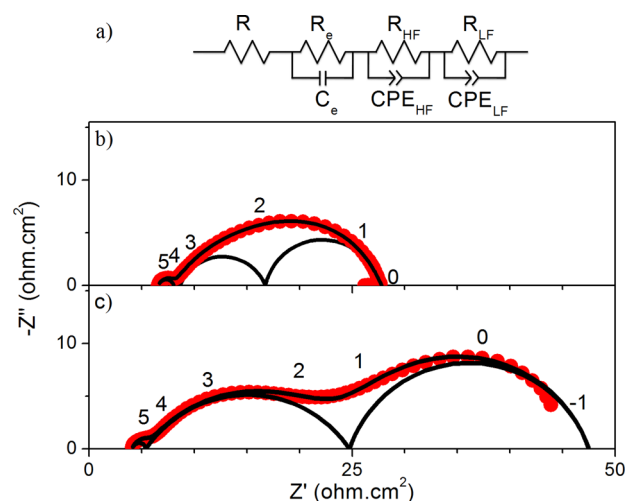

Figure 6. (a) Scheme of the equivalent circuit model employed to fit the EIS spectra of LSC-micro and -nano based cathodes. R: pure resistive contribution of the electrolyte. R_e and C_e: electrolyte's grain boundary resistance and capacitance. CPE: constant phase element. The two R//CPE subcircuits were used to fit the HF and LF arcs of the spectra. (b, c) Nyquist plots for LSC-nano and LSC-micro based cathodes, respectively. Red dots: experimental data. Black lines: Fitting function and contribution of each element circuit. Inserted numbers indicate the log(frequency) of each experimental point.

Table 9. Summary of Principal Results for LSC Cathodes Obtained from Equivalent Circuit Fitting Procedure onto EI Spectra Recorded at 500 °C

	LSC-micro	LSC-nano
f_p(Hz)[a] − HF[b]	380	204
f_p(Hz) − LF[c]	1.7	39
ASR$_{HF}$[d] (Ω·cm^2)	19.3(4)	8.1(4)
ASR$_{LF}$ (Ω·cm^2)	22.8(4)	10.8(3)
ASR$_{total}$ (Ω·cm^2)	42.1(9)	18.9(7)

[a]f_p: peak frequency. [b]HF: high frequency arc. [c]LF: low frequency arc. [d]ASR: area specific resistance.

Table 10. Activation Energies of Different Processes in LSC Cathodes from Arrhenius Plots

	E_a[a] (eV)	E_a (HF)[b] (eV)	E_a(LF)[c] (eV)
LSC-micro	1.58	1.39	1.85
LSC-nano	1.43	1.31	1.53

[a]E_a: total activation energy. [b]E_a (HF): activation energy of the high frequency process. [c]E_a (LF): activation energy of the low frequency process.

cathodes exhibit a depressed semicircle with $P = 0.9−0.99$ that was attributed to a double-layer-like process (DLL).[37] In the present case, it possibly takes place at the gas−cathode interface, as suggested by the relatively long characteristic time, τ_{LF}, which is on the order of ms.

When $P = 0.5$, a CPE element exhibits a straight line at 45° in the Nyquist plot, which is also the high frequency feature of the Finite Length Warburg (FLW) element, which, in turn, is a special case of the more realistic Generalized FLW. This element is commonly used to describe diffusion processes with a distribution of relaxation times.[37] This would be the case of the HF arc observed in LSC-micro.

Finally, a depressed arc with $0.6 < P < 0.8$ would be the result of multiple processes with close relaxation times and/or a

process with a distribution of relaxation times that may be originated in inhomogeneous material properties. This is the case of the LSC-micro LF arc and the LSC-nano HF arc which exhibit $P \approx 0.75$. To determine the kind of processes that are taking place in the cathode it is necessary to perform complementary studies. Tables 9 and 10 are organized in order to highlight the differences between the electrochemical performances of LSC-based cathodes.

Figure 7 shows Arrhenius plots for the ASRs of the different processes, in relation to the crystallite size of the starting
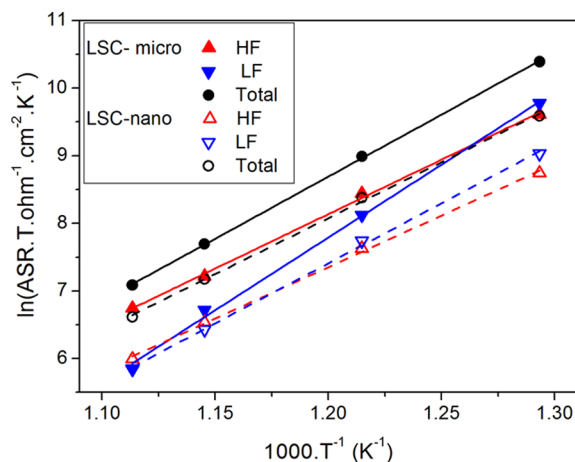

Figure 7. Arrhenius plots calculated from the ASR_{total} and from the ASRs of the high (HF) and low (LF) frequency arcs of LSC-micro and LSC-nano based cathodes. Straight lines: linear regression for the calculation of E_a.

powder and for the temperature range from 500 to 625 °C. Also compared are the total ASR values of the cathodes. From the slope of the straight line fitting it was possible to calculate the E_a of the different processes (Table 10). The E_a of the processes in LSC-micro are higher than in LSC-nano.

At 500 °C the small HF arc in Figure 6 can be fitted by an *RC* circuit, which has its time constant in the microsecond domain. Then, this arc could be ascribed to the electrolyte grain boundary diffusion process. The resistance and capacitance have nearly the same values in both cases, which also indicates that both electrolytes have the same properties in the two samples.

4. DISCUSSION

4.1. Structural Studies on LSC Powders. *4.1.1. Specific Considerations. First Shell.* Co K-edge XAS contains the contribution from all Co atoms excited by the X-ray source. So the XANES region will contain the contribution of all the illuminated Co species present in the sample. In the same way, the EXAFS signal is built up as the superposition of the contribution of all the local orders that exist in the sample. In accordance with this, a model is proposed in which there exists one different local order for each Co species, characterized by a particular Co–O bond length.

The model employed is intended to be in accordance with the crystal structure (SR-XRD) and Co speciation (XANES). Let us consider an ideal cubic perovskite with ABO_3 structure, with one Co^{3+} cation in the B-site and eight La^{3+} cations in the A-sites. As only 1/8 of each La^{3+} cation is in the cell, the sum over the 8 A-sites gives a total of one La^{3+} cation in the cell. Based on the unit cell neutrality condition, six O^{2-} anions must

fill the 3c sites of the $Pm\bar{3}m$ space group. As only one-half of each anion is in the cell, the sum gives a total of 3 O^{2-} anions inside the cell. Thus, each cell has a null charge.

On replacing La^{3+} by Sr^{2+} cations, the unit cell neutrality requires oxygen vacancy formation if cobalt cations remain in the +3 oxidation state.[38] Thus, in $La_{0.6}Sr_{0.4}CoO_{2.8}$ there will be 2.8 O^{2-} anions in the unit cell. So, how 2.8 anions can be accommodated in the unit cell is the key issue here. In an LSC crystal where all Co is in the +3 oxidation state and all unit cells are identical, it is clear that the only way to achieve 2.8 O^{2-} is by the oxygen vacancy formation process.

XANES analyses (LCF method) showed the presence of the three Co species in different specific amounts at high temperature in all the samples and also at RT in LSC-nano. A unit cell with a Co^{2+} cation must total to 2.3 O^{2-} in order to satisfy the unit cell neutrality condition. Another unit cell with a Co^{4+} cation must have 3.3 O^{2-}. As each anion is shared by two neighboring unit cells, to fulfill these requirements, 4.6, 5.6, or 6.6 oxygen anions would be needed surrounding the central cobalt in the +2, +3, or +4 oxidation states, respectively.

But there is another possibility. When the reduction of Co^{3+} to Co^{2+} is accompanied by the oxidation of another neighboring Co^{3+} to Co^{4+}, the whole process consists in a disproportionation reaction (also known as electronic compensation):

$$2Co^{3+} \rightarrow Co^{2+} + Co^{4+} \qquad (3)$$
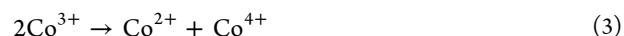
without the formation of an O^{2-} vacancy.[39] The key concept here is that it would be expected that the different charge on each Co species favors the displacement of an O^{2-} from the 3d site toward a Co^{4+} (Figure SI11), without the modification of the initial number (six) of oxygen atoms surrounding each cobalt atom.

Nevertheless, if the unit cell lattice parameter a remains constant during the oxygen displacement, then N_{occ} of the unit cell with Co^{2+} diminishes as the $Co^{2+}-O^{2-}$ bond elongates and the N_{occ} of the neighboring unit cell increases as $Co^{4+}-O^{2-}$ bond shortens, though $N_1 = 6$ for the two cobalt cations. In addition, the $Co^{3+}-O^{2-}$ bond length remains unchanged if the O^{2-} anion is located between two Co^{3+}. In this picture, the oxidation state of Co averaged over all unit cells remains unaltered and also the contribution of all unit cells will give the impression that all oxygen atoms are fixed in the 3d site of the cubic unit cell. In addition, the unit cell neutrality condition is satisfied by means of anion displacement along the Co–Co line or, equivalently, the unit cell's [100] direction of the cubic phase toward the most positively charged cation. This is in accordance with Chen et al.,[9] who observed this pathway near the 3d site by means of Rietveld refinements combined with the maximum entropy method. In other words, Chen et al. observed this pathway by the study of the long-range order, while the present work confirms that observation by studying the local atomic order of Co combined with XANES and SR-XRD and providing a more dynamical picture in which Co speciation plays a central role at intermediate temperatures.

XANES results show that this picture is possible. But they also suggest other possibilities taking place at the same time, as in all the cases and at 500 °C, the population of Co^{4+} is higher than that of Co^{2+} (Table 3). The simplest picture is that where a $V_O^{\bullet\bullet}$ is filled, the reaction
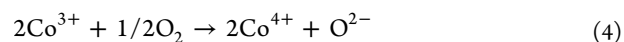
$$2Co^{3+} + 1/2O_2 \rightarrow 2Co^{4+} + O^{2-} \qquad (4)$$

Table 11. Relation between the Results Obtained by Means of the Different Studies (SR-XRD, XANES, and EXAFS)

sample	T °C	$d_{200/024}$[a] Å (SR-XRD)	d_{Co-O}[b] Å (SR-XRD)	COS[c] (XANES)	R_{Co-O}[d] Å (EXAFS)	N_1[e] (XANES)	N_{occ}[f]
LSC-micro	RT	1.9155(1)	1.925(1)	+3	1.928(6)	5.6	2.8
	500	1.93328(2)	1.93328(2)	+2	2.01(7)	5.9	2.7
				+3	1.94(2)		2.9
				+4	1.83(3)		3.3
LSC-nano	RT	1.91577(2)	1.921(2)	+2	1.91(1)	5.7	2.9
				+3			
				+4			
	500	1.93373(4)	1.93373(4)	+2	2.09(3)	5.7	2.4
				+3	1.93(4)		2.9
				+4	1.85(5)		3.1

[a]$d_{200/024}$: interplanar distance for (200) or (024) planes of the cubic or rhombohedral phase, respectively (SR-XRD). [b]Co−O distance calculated by means of SR-XRD analysis. [c]COS: Co oxidation state. [d]R_{Co-O}: Co−O bond length (EXAFS). [e]N_1: coordination number for the first coordination shell of Co, calculated from XANES analyses and unit cell neutrality condition. [f]N_{occ}: oxygen occupation number of the 3d site of a pseudocubic unit cell with a Co atom in the B-site.

takes place. In this scenario, as each cation has its particular ionic radius, then a particular R_{Co-O} is expected for each Co cation. This study shows that every R_{Co-O} is close to the expected value estimated from Shannon's work, where the influence of spin state on the ionic radius is also obvious.[30] In addition, the structure of the pre-edge peak in the Co K-edge XANES changes on going from LSC-micro to LSC-nano, and it is also sensitive to temperature changes (Figures SI4 and SI5).

Up to this point it is possible to see the complexity of the system and the consequent difficulty in building up a realistic model that takes into account all of these factors keeping, at the same time, a low number of variables during the EXAFS fitting procedure.

Nevertheless, among the perovskites, LSC particularly allows for such unique properties as those proposed: different valences are allowed for cobalt, even when the +3 and +4 oxidation states are not stable as individual oxides or equivalent compounds.[40] Related to this, the octahedral environment in the CoO$_6$ units that are found in the perovskite structure are flexible and can easily be accommodated into nominally less coordinated polyhedra, such as CoO$_5$ or CoO$_4$, contributing to the peculiar characteristics presented here.[41−43] The aliovalent Sr-induced vacancies find the perfect counterpart in multivalent cobalt for establishing important properties, such as mixed (electronic and ionic) conductivity, as (depending on temperature and oxygen partial pressure) Co^{4+} and oxygen vacancies can coexist and, more importantly, their relative concentrations naturally and nonarbitrarily adapt to the environmental variations. As a counterexample, Sr-doped Lanthanum manganites (LSM) do not exhibit this behavior, despite Mn being capable of the adoption of mixed valence states. This highlights the importance of the nature of the B-site transition element in perovskites, since its capability to cycle between oxidation states, coupled with its tendency to partially and momentarily adapt to different local symmetries, will determine significant changes in the material's reactivity.[38]

Table 11 summarizes the results obtained using this model in the EXAFS fitting procedure and their possible interpretation in terms of the SR-XRD and XANES analyses. The N_{occ} in a cubic (or pseudocubic) cell with lattice parameter a and N_1 oxygen atoms in the first shell for each cobalt species is also shown. The interplanar distance d_{200} of the family of planes {200} that alternatively contain Co/O and O/La/Sr atoms is also included. It represents the distance from the center (B-site) of the cubic unit cell to any of its faces. The difference observed

between d_{200} and d_{Co-O} is caused by the octahedra tilting in the rhombohedral phase. At 500 °C, where the cubic phase is present, there is no tilting of the octahedra and both parameters are equal.

In this picture, R_{Co-O} is shorter, almost equal to or longer than d_{200} depending on whether the B-site is occupied by Co^{4+}, Co^{3+}, or Co^{2+}, respectively. In order to maintain the unit cell neutrality condition, 3.3, 2.8, or 2.3 oxygen anions must be in a cell with Co^{4+}, Co^{3+}, or Co^{2+}, respectively, and N_{occ} is close to these numbers.

R_{Co-O} values at RT match d_{Co-O} values in all samples and increase with increasing D (Figure 5a). This is in accordance with the higher ϕ estimated for the LSC-micro powder. The presence of the different Co species at RT in LSC-nano may introduce distortions in the crystal lattice, making the rhombohedral distortions less noticeable than in the LSC-micro powder.

The Co^{3+}−O$^{2−}$ bond length is very similar to d_{Co-O} for all samples, probably because in all cases +3 is the predominant oxidation state and the minor contribution of the other two Co species to the SR-XRD patterns could be hidden by the peak width and the resolution of the experimental beamline setup and natural method limitation.

Second Shell. The changes in $\Delta d_{Co-La/Sr}$ as a function of D are another indication that rhombohedral distortions in nanostructured samples are less important than in microstructured powders. This is also observed in the local order, where there is no difference between R_{Co-Sr} and R_{Co-La} path lengths in LSC-nano, neither at RT nor at 500 °C.

Third Shell. In opposition to the expected thermal expansion effect at high temperature, observed by means of SR-XRD analyses, in the local order of Co such expansion is not seen. Instead, an apparent contraction of Co−Co paths is observed and it is more pronounced in LSC-nano.

4.1.2. General Considerations. The most important contribution of this work is that Co atoms in LSC powders exhibit the three possible oxidation states at IT-SOFC working temperatures. This fact, in turn, gives rise to the unexpected and very complex local order of Co atoms under those conditions.

Nevertheless, the different Co-ion distances are masked when analyzed using SR-XRD because, with these long-range order studies, an average Co-ion distance over all unit cells is obtained and the results thus support the cubic phase being present at high temperatures. This complex local order also

accounts for the mismatch observed between the SR-XRD patterns for LSC and the proposed structural models with the $R\bar{3}c$ or $Pm\bar{3}m$ space group symmetry.

The high defect concentration generated from the replacement of 40 mol % Sr^{2+} ($x = 0.4$) for La^{3+} (namely, Sr'_{La}, Co'_{Co}, $Co^{\bullet}_{Co}$, and $V^{\bullet\bullet}_{O}$) is expected to induce defect association.[47] These associations will in fact form new perovskite-like structures, very similar to that expected for LSC and very difficult to detect by SR-XRD. The randomly distributed vacancy model used here for the first coordination shell is related to the diluted vacancy model, applicable if $x < 0.01$. The reason that it works in these cases, where $x = 0.4$, may be that, as EXAFS is a local order probe, it really does not matter whether certain local order is uniformly mixed in the sample or whether it is part of a cluster formed by a unique type of local order. In addition, as coordination number possesses a high error when it is used as a fitting parameter, then a variation from 4.6 to 6 NN will not be critical and so we are able to use a unique average value for the three local orders proposed here.

In LSC-micro powders, the coexistence of the three Co species is a thermally activated feature as, at RT, all Co atoms are in the +3 oxidation state but, with increasing temperature, a part of them changes to the +2 or +4 oxidation states. But it is the crystallite size effect on the nanostructured powder what changes Co local order and Co speciation in a similar way as temperature does on microstructured powder (Tables 6 and 7). These facts first show the capability of cobalt atoms to easily change their oxidation state in response to changes in temperature or because of surface effects (such as defect concentration) in nanocrystalline powders. Second, if this capability is responsible for the MIEC properties of LSC, then it explains the enhanced ionic conduction and surface activity of LSC-nano, as the features that give rise to those properties are present at temperatures as low as 20 °C. The appearance of the first shell splitting into three subshells should also play an important role in these properties as, as well as inducing oxygen octahedra distortions, oxygen anions bonded to Co^{2+} cations are less tightly bonded than the others because of both the longer bond and the lower strength of the electric field of Co^{2+}, allowing them to move more freely.

One fact that stands out is that the DW factor decreases at high temperature for the LSC-nano sample. It is also smaller than the DW factor of the LSC-micro powder at the same temperature. It seems that, as $R_{Co-La/Sr}$ and R_{Co-Co} shorten from RT to 500 °C, La^{3+} and Sr^{2+} cations have less free space to move around an equilibrium position as the consequence of thermal excitation. This also explains why the DW factor is lower for Sr^{2+} than for La^{3+} cations, as the former have a larger ionic radius (1.44 vs 1.36 Å).[30] Beyond these speculations, it has to be taken into account that these quite unexpected results are more likely to be the consequence of trying to fit the very complex scenario of the second and third shells to a simple model.

The expected effect on thermal properties when going from the microscale to the nanoscale domain, such as enhanced thermal conductivity due to the larger SSA and the higher fraction of atoms on the surface, could possibly be enhanced in the case of perovskites.[44−46] The cited effects on thermal properties would be more pronounced for the LSC-nano sample and would explain the differences in the EXAFS results at different temperatures, going from the microscale (LSC-micro) to the nanoscale (LSC-nano) domain. The differences

in the local order and the chemical properties of Co in LSC will affect the MIECs properties and redox activity of LSC-nanobased cathodes.

4.2. Electrochemical Performance. Preliminary EIS studies showed a better performance of LSC-nano cathodes taking into account that both the ASR and E_a are lower than in LSC-micro cathodes. Nevertheless, comparing ASR values is quite difficult as, for the normalization, the painted area is used instead of the real area of the cathode's surface exposed to the gas phase. In MIECs this is an important issue because the entire cathode surface has active sites for the ORR. So, a lower ASR value in nanostructured cathodes could be the result of an underestimated surface area instead of a real cathode performance improvement. Thus, it is better to compare some other parameters such as, for example, the characteristic time, $\tau = RC$, of each type of process.

Regarding the use of $R//CPE$ elements in this first approach, CPE exhibiting low P values does not give any physical information about the processes taking place in the cathode, cathode/electrolyte or gas/cathode interface. Only in the case where $0.9 < P < 0.99$ would it be ascribed to a double layer process in a rough or porous cathode but, to confirm this, further experimental background and data analysis are required.[37] The value of these EIS measurements lies in that they show that crystallite size does affect the electrochemical performance of LSC cathodes. Taking into account the f_p, the HF arc would correspond to the charge transfer process at the cathode/electrolyte interface. The surface reactions on the LSC cathode, in turn, would be responsible for the LF arc. In any case, the LF limiting process in LSC-nano based cathode is faster and could be linked to the cobalt speciation and its local order, as will be explained below.

XAS and SR-XRD studies show that the crystallite size does affect the chemical and structural properties of the Co atom in LSC as it exhibits, in the LSC-nano powder, its three possible oxidation states at RT in a proportion close to that exhibited by LSC-micro at high temperature. Moreover, at 500 °C, they are almost equal to the proportions observed at 700 °C in LSC-micro. This could be interpreted as an enhanced ease of Co to change its oxidation state in LSC-nano. This feature could be linked to the improvement in the performance of the LSC-nanobased cathode, as observed in its LF arc which has a higher f_p. This is possible because the procedure employed to fabricate the symmetrical cells does not change the original properties of the starting powders. The mentioned cobalt properties could also explain the speed up of the diffusion process observed in another LSC-nano based cathode, in the work of Acuña et al.[16] It is possible that both electronic current and vacancy transport requires that the Co atoms change their oxidation state locally, generating appropriate electronic conduction bands and also local dipole moments that pull oxide anions through the material.

The existence of more Co^{4+} than Co^{2+} may be associated with the high activity for the ORR because, when temperature increases, LSC powders gain oxygen atoms from the surrounding air. Then, its ability for conducting oxygen atoms and releasing them at the electrode−electrolyte interface is possibly related to the ease with which the Co atom changes its oxidation state.

The presence of Co^{3+} and Co^{4+} in LSC-nano accounts for the mixed compensation of the acceptor which, in part, generates oxygen vacancies, $V^{\bullet\bullet}_{O}$, and also promotes Co^{3+} oxidation. In Kröger-Vink notation this is represented as

$$[Sr'_{La}] = 2[V_O^{\bullet\bullet}] + [Co_{Co}^{\bullet}] \qquad (5)$$

The presence of Co^{2+} assures the production of electrons along with more oxygen vacancies.[38]

$$[Co'_{Co}] = 2[V_O^{\bullet\bullet}] \qquad (6)$$

Also, the presence of Co^{2+} and Co^{4+} could be related to a change in the oxidation state of Co^{3+}, in the way stated by the equation

$$2Co_{Co}^{X} = Co'_{Co} + Co_{Co}^{\bullet} \qquad (7)$$

which is schematized in Figure SI11.

Linking both the cathode performance and the fitting results of the EI spectra with these equations makes it clear that oxygen vacancies play an important role in oxygen diffusion, as stated by numerous previous studies. Here, as Co^{2+} population is almost equal in both samples, in LSC-nano there is more Co^{3+} than Co^{4+}, which means (looking at eq 5) that a higher oxygen vacancy concentration is present in the nanomaterial. This may favor the oxygen diffusion process.

It would be interesting to determine the role of the Co^{2+} cation in surface activity in the LSC cathode. As it has the lowest ionization energy, it would be expected to promote the oxygen reduction at the LSC cathode surface.

Another interesting issue is the influence that the Ag current collector would have on the cathode's electrochemical performance and the role it plays beyond the expected electronic conduction. Particularly, it will be important to know if the cathode-current collector interaction is modified by the different chemical properties of cobalt atoms in LSC-nano and LSC-micro cathodes or by their crystallite or grain size. Nevertheless, it should be clear that, in any case, the changes in the electrochemical performance observed in this work are attributable to the crystallite size effect on LSC powders, as the procedure employed to fabricate the symmetrical cells were the same in both cases.

In relation to cathode performance, a slightly different technique for slurry preparation and deposition onto the electrolyte surface is currently under study, in order to optimize the cathode microstructure. In addition, it is important to determine the optimal sintering temperature of the cathode prepared from either nanostructured or microstructured LSC starting powders. Also, in each case the cathode's thickness should be optimized.

5. CONCLUSIONS

Using the linear combination method for fitting the Co K-edge XANES spectra with proper standards for the different Co oxidation states made possible for the first time the quantification, in relation to these reference standards, of the relative abundance of cobalt in +2, +3, or +4 oxidation states in LSC powders of 30 nm average crystallite size and in microcrystalline LSC powders at RT and at 500 °C. In the latter it was also possible to calculate this ratio when the sample was heated up to 700 °C.

In the LSC microcrystalline powder, Co atoms are all in the +3 oxidation state at RT, and the three cobalt species are present at high temperature, in amounts that varied with temperature, while the average oxidation state of Co did not change significantly. On the other hand, nanostructured LSC powder exhibited the three Co species at RT and, at 500 °C, they were present in proportions very similar to those exhibited by microstructured LSC at 700 °C. These features could be a

consequence of crystallite size effects, as no other parameter differs from one powder to the other (such as different synthesis method, calcining conditions other than temperature or measurements conditions, among others).

The existence of the three cobalt species distorts the expected Co local order, creating pathways for oxygen diffusion. At 500 °C, the population of Co in +2 and +4 oxidation states in nanostructured LSC is bigger than in microstructured LSC, making cobalt local order distortions more pronounced. These distinctions may have profound consequences on the LSC cathode activity as the nanostructured-based cathode exhibits an enhanced electrochemical performance, observed as an increase in the rate of a specific (undetermined) low frequency process. Also, the ASR and activation energies of the limiting processes in the nanostructured LSC cathode are lower than in the microstructured LSC cathode.

The fact that the average Co oxidation state is +3 from RT to high temperature ($\leq$700 °C) in both samples means that the number of oxygen vacancies is essentially constant in this interval. So we propose that Co speciation and local order distortions are the key features that rule the electrochemical activity of the LSC and may control the oxygen reduction reaction and oxygen diffusion, among other processes, in the cathode.

■ ASSOCIATED CONTENT

ⓢ Supporting Information

The Supporting Information is available free of charge on the ACS Publications website at DOI: 10.1021/acs.jpcc.6b06622.

> SEM images of LSC precursor ashes and products after calcination at 600 and 1100 °C. SR-XRD patterns of LSC-nano at RT and 500 °C. Co K-edge XANES of CoO, $LaCoO_3$ and $BaCoO_3$ standards. Pre-edge structure of Co K-edge XANES of LSC-micro and -nano at RT, 500, and 700 °C, and of Co(II), Co(III), and Co(IV) standards at RT. EXAFS signal and fitting function in k-, R-, and q-space for LSC powders at RT and 500 °C. Scheme of the oxygen displacement due to electronic compensation (PDF).

■ AUTHOR INFORMATION

Corresponding Author

*Tel./Fax: +54 11 4709 8158. E-mail: lacuna@citedef.gob.ar.

Notes

The authors declare no competing financial interest.

■ ACKNOWLEDGMENTS

■ REFERENCES

(1) Tokura, Y.; Nagaosa, N. Orbital Physics in Transition-Metal Oxides. *Science* **2000**, *288*, 462−468.

(2) Elemans, J. B. A. A.; van Laar, B.; van der Veen, K. R.; Loopstra, B. O. The Crystallographic and Magnetic Structures of $La_{1−x}Ba_xMn_{1−x}Me_xO_3$ (Me = Mn or Ti). *J. Solid State Chem.* **1971**, *3*, 238−242.

(3) Norby, P.; Krogh Andersen, I. G.; Krogh Andersen, E.; Andersen, N. H. Crystal Structure of Lanthanum Manganate(III), $LaMnO_3$, at Room Temperature and at 1273 K under N_2. *J. Solid State Chem.* **1995**, *119*, 191−196.

(4) Skinner, S. J. Recent Advances in Perovskite-type Materials for Solid Oxide Fuel Cell Cathodes. *Int. J. Inorg. Mater.* **2001**, *3*, 113−121.

(5) Mineshige, A.; Kobune, M.; Fujii, S.; Ogumi, Z.; Inaba, M.; Yao, T.; Kikuchi, K. J. Metal-Insulator Transition and Crystal Structure of $La_{1-x}Sr_xCoO_3$ as Functions of Sr-Content, Temperature, and Oxygen Partial Pressure. *J. Solid State Chem.* **1999**, *142*, 374−381.

(6) Adler, S. B. Mechanism and Kinetics of Oxygen Reduction on Porous $La_{1-x}Sr_xCoO_{3-\delta}$ Electrodes. *Solid State Ionics* **1998**, *111*, 125−134.

(7) Nielsen, J.; Hjalmarsson, P.; Hangaard Hansen, M.; Blennow, P. Effect of Low Temperature in-situ Sintering on the Impedance and the Performance of Intermediate Temperature Solid Oxide Fuel Cell Cathodes. *J. Power Sources* **2014**, *245*, 418−428.

(8) De Souza, R. A.; Kilner, J. A. Oxygen Transport in $La_{1-x}Sr_xMn_{1-y}Co_yO_{3-\delta}$. *Solid State Ionics* **1998**, *106*, 175−187.

(9) Chen, Y.-C.; Yashima, M.; Ohta, T.; Ohoyama, K.; Yamamoto, S. Crystal Structure, Oxygen Deficiency and Oxygen Diffusion Path of Perovskite-type Lanthanum Cobaltites $La_{0.4}Ba_{0.6}CoO_{3-\delta}$ and $La_{0.6}Sr_{0.4}CoO_{3-\delta}$. *J. Phys. Chem. C* **2012**, *116*, 5246−5254.

(10) Bansal, N. P.; Zhong, Z. Combustion Synthesis of $Sm_{0.5}Sr_{0.5}CoO_{3−x}$ and $La_{0.6}Sr_{0.4}CoO_{3−x}$ Nanopowders for Solid Oxide Fuel Cell Cathodes. *J. Power Sources* **2006**, *158*, 148−153.

(11) Hayd, J.; Dieterle, L.; Guntow, U.; Gerthsen, D.; Ivers-Tiffée, E. Nanoscaled $La_{0.6}Sr_{0.4}CoO_{3−\delta}$ as Intermediate Temperature Solid Oxide Fuel Cell Cathode: Microstructure and Electrochemical Performance. *J. Power Sources* **2011**, *196*, 7263−7270.

(12) Heel, A.; Holtappels, P.; Graule, T. On The Synthesis and Performance of Flame-made Nanoscale $La_{0.6}Sr_{0.4}CoO_{3−\delta}$ and Its Influence on the Application as an Intermediate Temperature Solid Oxide Fuel Cell Cathode. *J. Power Sources* **2010**, *195*, 6709−6718.

(13) Orikasa, Y.; Ina, T.; Nakao, T.; Mineshige, A.; Amezawa, K.; Oishi, M.; Arai, H.; Ogumi, Z.; Uchimoto, Y. X-ray Absorption Spectroscopic Study on $La_{0.6}Sr_{0.4}CoO_{3-\delta}$ Cathode Materials Related with Oxygen Vacancy Formation. *J. Phys. Chem. C* **2011**, *115*, 16433−16438.

(14) Ovenstone, J.; White, J. S.; Misture, S. T. Phase Transitions and Phase Decomposition of $La_{1-x}Sr_xCoO_{3-\delta}$ in Low Oxygen Partial Pressures. *J. Power Sources* **2008**, *181*, 56−61.

(15) Sacanell, J.; Leyva, A. G.; Bellino, M. G.; Lamas, D. G. Nanotubes of Rare Earth Cobalt Oxides for Cathodes of Intermediate-Temperature Solid Oxide Fuel Cells. *J. Power Sources* **2010**, *195*, 1786−1792.

(16) Acuña, L. M.; Peña-Martínez, J.; Marrero-López, D.; Fuentes, R. O.; Núñez, P.; Lamas, D. G. Electrochemical Performance of Nanostructured $La_{0.6}Sr_{0.4}CoO_{3-\delta}$ and $Sm_{0.5}Sr_{0.5}CoO_{3-\delta}$ Cathodes for IT-SOFCs. *J. Power Sources* **2011**, *196*, 9276−9283.

(17) Shao, Z.; Zhou, W.; Zhu, Z. Advanced Synthesis of Materials for Intermediate-Temperature Solid Oxide Fuel Cells. *Prog. Mater. Sci.* **2012**, *57*, 804−874.

(18) Liu, B.; Zhang, Y.; Zhang, L. Characteristics of $Ba_{0.5}Sr_{0.5}Co_{0.8}Fe_{0.2}O_{3−\delta}$−$La_{0.9}Sr_{0.1}Ga_{0.8}Mg_{0.2}O_{3−\delta}$ Composite Cathode for Solid Oxide Fuel Cell. *J. Power Sources* **2008**, *175*, 189−195.

(19) Taguchi, H.; Yamada, S.; Nagao, M.; Ichikawa, Y.; Tabata, K. Surface Characterization of $LaCoO_3$ Synthesized Using Citric Acid. *Mater. Res. Bull.* **2002**, *37*, 69−76.

(20) Milt, V. G.; Ulla, M. A.; Miró, E. E. NO_x Trapping and Soot Combustion on $BaCoO_{3-y}$ Perovskite: LRS and FTIR Characterization. *Appl. Catal., B* **2005**, *57*, 13−21.

(21) Furlan Ferreira, F.; Correa, H. P. S.; Orlando, M. T. D.; Passamai, J. L., Jr; Orlando, C. G. P.; Cavalcante, I. P.; Garcia, F.; Tamura, E.; Martinez, L. G.; Rossi, J. L.; et al. Pressure Study of Monoclinic ReO_2 up to 1.2 GPa Using X-ray Absorption Spectroscopy and X-ray Diffraction. *J. Synchrotron Radiat.* **2009**, *16*, 48−56.

(22) Schmitt, B.; Brönnimann, Ch.; Eikenberry, E. F.; Gozzo, F.; Hörmann, C.; Horisberger, R.; Patterson, B. Mythen Detector System. *Nucl. Instrum. Methods Phys. Res., Sect. A* **2003**, *501*, 267−272.

(23) Rodríguez-Carvajal, J. *Program FullProf.2k*, Version 5.20 − Jul. 2011-ILL JRC; Laboratoire Léon Brillouin (CEA-CNRS), France, 2011.

(24) Tolentino, H.; Cezar, J. C.; Cruz, D. Z.; Compagnon-Cailhol, V.; Tamura, E.; Martins Alves, M. C. Commissioning and First Results of the LNLS XAFS Beamline. *J. Synchrotron Radiat.* **1998**, *5*, 521−523.

(25) Kelly, S. D.; Hesterberg, D.; Ravel, B. *Methods of Soil Analysis*; Soil Science Society of America: Madison, U.S.A., 2008.

(26) Ressler, T. WinXAS: a Program for X-ray Absorption Spectroscopy Data Analysis under MS-Windows. *J. Synchrotron Radiat.* **1998**, *5*, 118−122.

(27) Newville, M.; Ravel, B.; Haskel, D.; Rehr, J. J.; Stern, A.; Yacoby, Y. Analysis of Multiple-Scattering XAFS Data Using Theoretical Standards. *Phys. B* **1995**, *208-209*, 154−156.

(28) Ankudinov, A. L.; Ravel, B.; Rehr, J. J.; Conradson, S. D. Real-Space Multiple-Scattering Calculation and Interpretation of X-Ray-Absorption Near-Edge Structure. *Phys. Rev. B: Condens. Matter Mater. Phys.* **1998**, *58*, 7565−7576.

(29) Ravel, B. ATOMS: Crystallography for the X-ray Absorption Spectroscopist. *J. Synchrotron Radiat.* **2001**, *8*, 314−316.

(30) Shannon, R. D. Revised Effective Ionic Radii and Systematic Studies of Interatomie Distances in Halides and Chaleogenides. *Acta Crystallogr., Sect. A: Cryst. Phys., Diffr., Theor. Gen. Crystallogr.* **1976**, *32*, 751−767.

(31) Altermatt, D.; Brown, I. D. The Automatic Searching for Chemical Bonds in Inorganic Crystal Structures. *Acta Crystallogr., Sect. B: Struct. Sci.* **1985**, *41*, 240−244.

(32) Brown, I. D.; Altermatt, D. Bond-Valence Parameters Obtained from a Systematic Analysis of the Inorganic Crystal Structure Database. *Acta Crystallogr., Sect. B: Struct. Sci.* **1985**, *41*, 244−247.

(33) Adams, S.; Swenson, J. Pathway Models for Fast Ion Conductors by Combination of Bond Valence and Reverse Monte Carlo Methods. *Solid State Ionics* **2002**, *154−155*, 151−159.

(34) Young, R. A. *The Rietveld Method*; Oxford University Press: Oxford, U.K., 1993.

(35) de Groot, F.; Vankó, G.; Glatzel, P. The 1s X-ray Absorption Pre-Edge Structures in Transition Metal Oxides. *J. Phys.: Condens. Matter* **2009**, *21*, 104207.

(36) Ross Macdonald, J. Note on the Parameterization of the Constant-Phase Admittance Element. *Solid State Ionics* **1984**, *13*, 147−149.

(37) Ross Macdonald, J. *Impedance Spectroscopy Theory, Experiment, and Applications*; John Wiley & Sons, Inc.: New Jersey, U.S.A., 2005.

(38) Kilner, J. A.; Berenov, A.; Rossiny, J. Diffusivity of the Oxide Ion in Perovskite Oxides. In *Perovskite Oxide for Solid Oxide Fuel Cells*; Ishihara, T., Ed.; Springer Science Business Media: New York, U.S.A., 2009.

(39) Raveau, B.; Seikh, Md. M. *Cobalt Oxides: From Crystal Chemistry to Physics*; Wiley-VCH: New Jersey, U.S.A., 2012.

(40) Kawada, T. Perovskite Oxide for Cathode of SOFCs. In *Perovskite Oxide for Solid Oxide Fuel Cells*; Ishihara, T., Ed.; Springer Science Business Media: New York, U.S.A., 2009.

(41) Irvine, J. T. S. Perovskite oxide anodes for SOFCs. In *Perovskite Oxide for Solid Oxide Fuel Cells*; Ishihara, T., Ed.; Springer Science Business Media: New York, U.S.A., 2009.

(42) Thursfield, A.; Kruth, A.; Irvine, J. T. S.; Metcalfe, I. S. Defect Chemistry and Transport in Metal Oxides. In *Metal Oxides: Chemistry and Applications*; Fierro, J. L. G., Ed.; CRC Press: Florida, U.S.A., 2006.

(43) Verma, A. S.; Jindal, V. K. ABX_3-Type Oxides and Halides: Their Structure and Physical Properties. In *Perovskites: Structure,*

Properties and Uses; Borowski, M., Ed.; Nova Science Publishers, Inc.: New York, U.S.A., 2010.

(44) Das, S. K.; Choi, S. U. S.; Yu, W.; Pradeep, T. *Nanofluids: Science and Technology*; John Wiley & Sons, Inc.: New Jersey, U.S.A., 2007.

(45) Huber, C. A. X-ray Diffraction Characterization of Nanophase Materials. In *Handbook of Nanophase Materials*; Goldstein, A. V., Ed.; Marcel Dekker, Inc.: New York, U.S.A., 1997.

(46) Ishihara, T., Ed. Structure and Properties of Perovskite Oxides. In *Perovskite Oxide for Solid Oxide Fuel Cells*; Springer Science Business Media: New York, U.S.A., 2009.

(47) Petrov, A. N.; Kononchuk, O. F.; Andreev, A. V.; Cherepanov, V. A.; Kofstad, P. Crystal Structure, Electrical and Magnetic Properties of $La_{1-x}Sr_xCoO_{3-y}$. *Solid State Ionics* **1995**, *80*, 189−199.